43rd AIAA Plasmadynamics and Lasers Conference
25-28 Jun 2012, New Orleans, LS
AIAA-2012-2985

Comparison of Aero-Optical Measurements from the Flight Test of Full and Hemispherical Turrets on the Airborne Aero-Optics Laboratory

Nicholas De Lucca[1], Stanislav Gordeyev[2], and Eric Jumper[3]
University of Notre Dame, Notre Dame, Indiana, 46545

The optical environment around both a hemisphere-on-cylinder turret and a hemisphere-only turret with flat and conformal windows was characterized at both subsonic and transonic speeds. Data was taken from Mach 0.4 to 0.65 at altitudes from 15,000 ft to 30,000 ft to analyze scaling laws, with a focus on Mach numbers of 0.5 and 0.65. A 25 kHz Shack-Hartmann wavefront sensor was used to measure the optical aberrations around the turret. Data were primarily collected while the two planes slewed by, giving statistics at several azimuthal/elevation angles with additional data taken at fixed angles. Additionally, dynamics of a local shock appearing on the conformal-window turret at the transonic Mach number are presented and discussed.

I. Introduction

The turret geometry is common in directed energy applications as it provides excellent field-of-regard. However, for flight situations at a Mach number of 0.3 or larger, this geometry introduces a complex, highly three-dimensional turbulent flow [1]. The turbulent flow induces density fluctuations that cause substantial unsteady aberrations in the projected laser [2], referred to as aero-optical effects [3]. These aberrations limit the effective field-of-regard of the projection system. The density of air is related to its index of refraction through the Gladstone-Dale relation, $n(x,y,z,t)-1=K_{GD}\rho(x,y,z,t)$. For air with any density gradients, the index of refraction in not constant, and an incident planar wavefront will be distorted. For turbulent flow, the distortions are a function of both position and time. The Optical Path Length, OPL, is the integrated value of the index of refraction along a path through the fluid, $OPL(x,y,t)=\int_{s1}^{s2} n(x,y,z,t)ds$. The wavefront deviation from the mean value is characterized by the Optical path Difference, $OPD(x,y,t)=OPL(x,y,t)-\overline{OPL(x,y,t)}$. The optical path difference is the conjugate of the wavefront, $OPD=-W$.

The canonical turret typically has the hemisphere-on-cylinder geometry. To study effect of the turret height on the aero-optical aberrations, the hemisphere-only turret will also be discussed in this paper. The flow around the hemisphere-on-cylinder turret has been intensively studied before [4,5]. A depiction of the significant flow features is given in figure 1. The incoming flow stays attached over the top of the turret on the upstream half. Over the downstream or the aft half of the turret, the curvature of the turret induces an adverse pressure gradient that eventually causes separation. The separated wake region of the turret is comprised of two horn vortices. Additionally, a necklace vortex forms near the base of the turret and extends downstream on both sides of the turret. For turrets with a flat

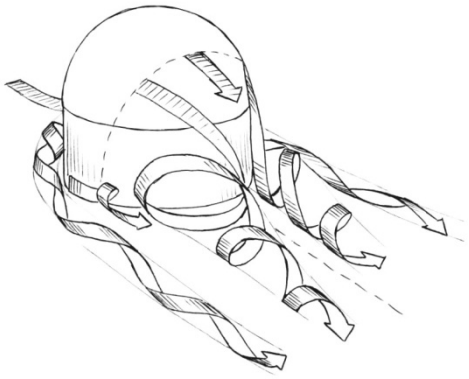

Figure 1. The flow structures around a hemisphere-on-cylinder turret.

[1] Graduate Student, Department of Mechanical and Aerospace Engineering, Hessert Laboratory for Aerospace Research, Notre Dame, IN 46556, Student Member.
[2] Research Associate Professor, Department of Mechanical and Aerospace Engineering, Hessert Laboratory for Aerospace Research, Notre Dame, IN 46556, Senior AIAA Member.
[3] Professor, Department of Mechanical and Aerospace Engineering, Hessert Laboratory for Aerospace Research, Notre Dame, IN 46556, AIAA Fellow.

window instead of a conformal window, the flow separates prematurely at the leading edge of the slope discontinuity of the flat window for a range of side-looking angles [4,11], creating additional aero-optical effects. The hemisphere-only turret has similar flow structures to the full hemisphere-on-cylinder turret [1].

The AAOL Program exists as a flight-testing platform for aero-optical studies. The program conducts extensive investigation of aero-optical characteristics of flows around turrets [3,4]. The aircraft has also been modified to investigate in-flight aero-optical properties of boundary layers. AAOL data has also been used as a test case for AO systems [7]. See [8] for a more comprehensive description of the AAOL platform.

Recently, additional CFD studies on both flat and conformal window turret configurations at subsonic and transonic speeds have also been performed [6], where flow fields around a hemisphere-only turret and a submerged hemisphere turret were computed and compared. It was shown that, on one end, altering turret geometry can reduce the size of the necklace vortex, but on the other end, it might have a larger effect on aero-optical distortions at forward-looking angles as the aperture will be closer to the vortical structures near the bottom of the turret; the same is true of the full hemisphere-on-cylinder turret and the hemisphere-only turret. The studies also revealed the formation of more than one necklace vortex at transonic speeds for the hemispherical turret. Lastly, density fluctuations have been computed along the turret, to attempt to estimate aero-optical performance. It was shown that the hemispherical turret performed better than the submerged hemisphere in the transonic regime and vice-versa in the subsonic regime. This indicates that an optimal turret geometry for all flight situations does not exist, and design must be directed to specific desired flow regimes.

II. Experimental Setup

The AAOL program consists of two aircraft: one lead aircraft that contains the turret assembly and instrumentation and a secondary chase aircraft that projects a laser onto the turret. Below only essential information about AAOL is provided, the reader is referred to [8] for a detailed description and capabilities of the AAOL platform. The aircraft with the turret and the aircraft with the laser will be referred to as the laboratory aircraft and the laser aircraft, respectively. The two aircraft fly in close formation, with a nominal separation of 50 meters. In the laboratory aircraft, the turret assembly is mounted to an optical table and protrudes out of a modified escape hatch. The escape hatch can also be integrated with additional measurement devices, such as Pitot rakes. The laser is projected through a window on the laser aircraft onto the pupil of the turret, preventing propagation through non-boundary-layer turbulence before the laser reaches the turret. The laser emerges as a diverging beam overfilling the turret aperture on the laboratory plane by a factor of two. Figure 2, below, shows the turret in both the hemispherical and full turret configurations.

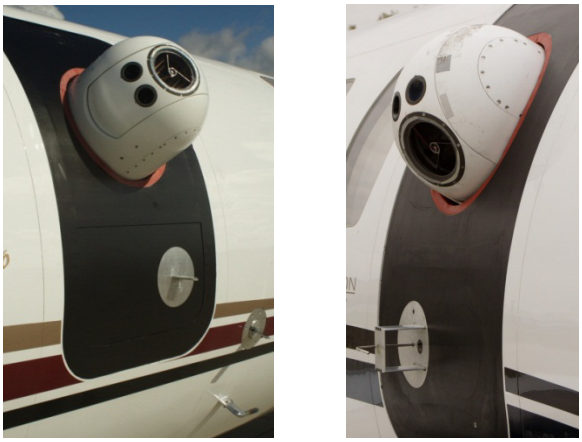

Figure 2. The AAOL turret, as a full hemisphere-on-cylinder turret, left and a hemisphere-only turret, right.

The optical setup and instrumentation are shown in Figure 3. The primary sensor on the laboratory aircraft is a high speed Shack-Hartmann wavefront sensor, capable of acquiring 32x32 sub-apertures at 25 kHz for 21000 frames. A closed-loop, Fast Steering Mirror (FSM) system in the turret assembly stabilizes the beam on the sensor. Residual beam jitter is measured with a position sensing device (PSD). Additional data acquired includes the instantaneous flight speed, static/total pressures and turret elevation and azimuthal angles. The instantaneous separation of the two aircraft is recorded via differential GPS. The jitter data and flight conditions were acquired at 100 kHz, while the GPS data was collected with a separate, yet synchronized system. Wavefronts were acquired

separately; the wavefront sensor was synchronized with the jitter collection. Jitter and GPS data will not be presented in this paper.

Wavefront data were acquired in two different flight modes: a fixed position and a "slew" maneuver. Fixed-position wavefronts were acquired at 25 kHz for 0.6 seconds to collect time-resolved wavefronts of the aero-optical structures. Slewing maneuvers involve the laboratory aircraft holding position while the laser aircraft slowly and monotonically changes position with respect to it. For the slewing maneuver, the wavefront sampling rate was reduced to 3 kHz and data were acquired over 7 seconds to collect wavefront data over a range of viewing angles. The slewing maneuvers allow efficient collection of aero-optical statistical quantities over a large range of azimuth and elevation angles, allowing for rapid mapping of the aero-optical performance of the turret.

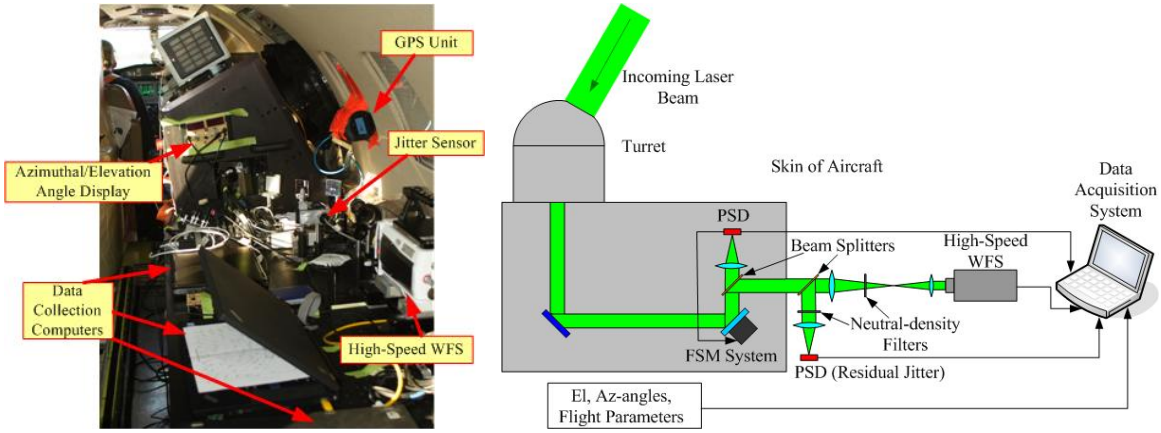

Figure 3. The experimental setup on the laboratory aircraft.

III. Data Reduction

Processed data from the high-speed wavefront sensor is of the form of a time-sequence of two-dimensional wavefront data, $W = W(x, y, t)$. From this sequence, instantaneous tip/tilt and piston components were all removed. The time-average wavefront for each sub-aperture, that is a steady lensing, was also removed from each wavefront. For slewing maneuvers, wavefront time series were split into 0.5-second blocks, and the steady lensing of each block was removed while the fixed point data sets were treated as a single block. Dividing data into small-duration blocks of the slewing maneuver ensures correct converged statistics at series of discrete flight angles during each maneuver, while the turret angle stays approximately constant for each data block. To characterize the optical performance of the turret at a given set of viewing angles, several statistics of the OPD are computed. The amount of aberration across the entire aperture at a given angle and instant in time is quantified by $OPD_{RMS}(t) = \sqrt{\langle OPD(x,y,t)^2 \rangle_{x,y}}$ with the angle brackets denoting spatial averaging. The time-average of this quantity, later referred to as OPD_{RMS}, gives the average value of the aero-optical distortions at a given angle. Additionally, it is useful to quantify the spatial distribution of optical distortions, later referred to as the spatial distribution of OPD_{RMS}, $OPD_{RMS}(x, y) = \sqrt{\overline{OPD(x,y,t)^2}}$.

IV. Results

For the comparison of full and hemispherical turrets, with both flat and conformal windows, OPD_{RMS} was computed over a wide range of viewing angles. To allow comparison of data at different flight conditions, OPD_{RMS} is normalized,

$$OPD_{Norm}\left(\frac{\mu m}{m}\right) = \frac{OPD_{RMS}}{\frac{\rho}{\rho_{SL}} M^2 D}.$$

Here the free stream density is ρ, the density at sea level is ρ_{SL}, the Mach number is given by M and the turret diameter is D. This scaling has been demonstrated to normalize aero-optical distortions over a range of subsonic Mach numbers up to 0.5 [4]. Additionally, the coordinate system for data presentation is re-defined from the traditional azimuth and elevation angle system. Instead, data are presented as a function of viewing angle and

modified elevation angle. These new angles are defined by $\alpha = \cos^{-1}\left(\cos(Az)\cos(El)\right)$ and $\beta = \tan^{-1}\left(\frac{\tan(El)}{\sin(Az)}\right)$, with α being the viewing angle and β the modified elevation angle [1].

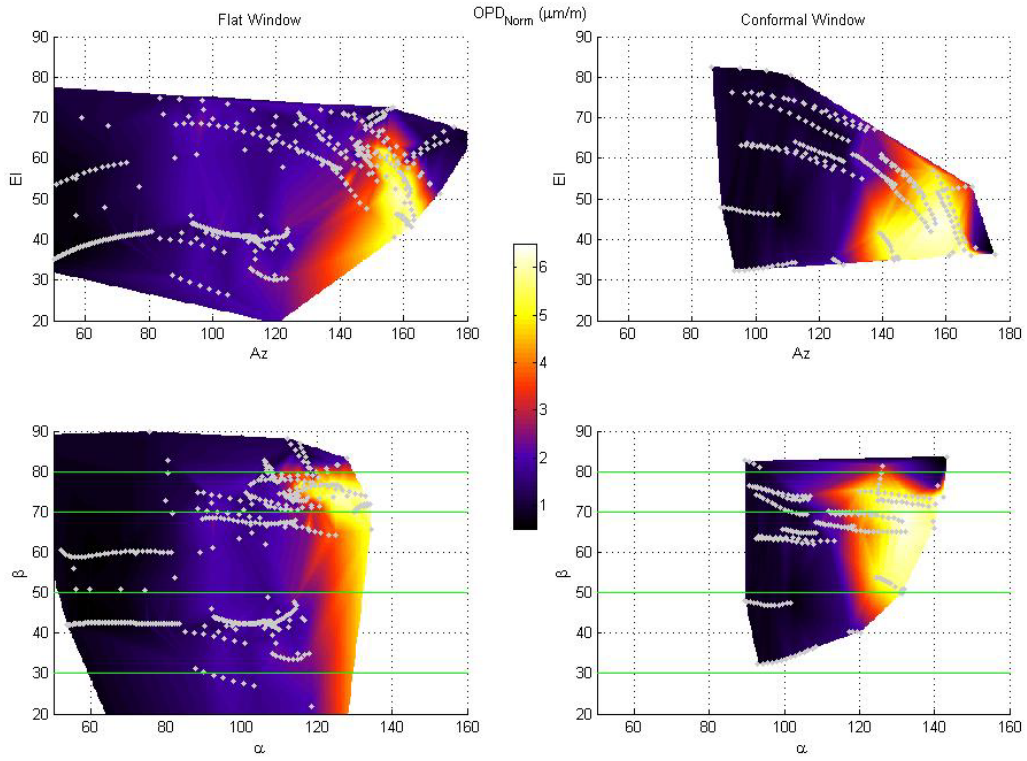

Figure 4. Maps of OPD_{RMS} as a function of both azimuth and elevation angles and viewing and modified elevation angles frame-of-references for the full hemisphere-on-cylinder turret in subsonic flow.

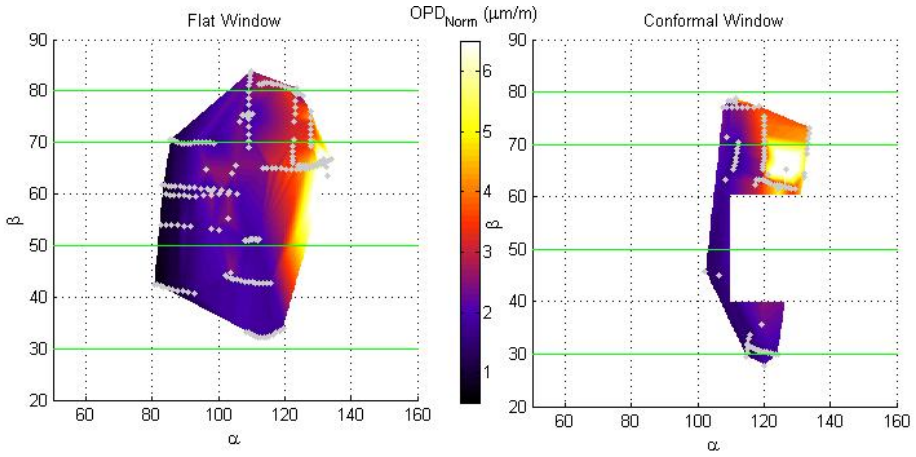

Figure 5. Maps of OPD_{RMS} as a function of viewing and modified elevation angles for the hemisphere-only turret in subsonic flow.

Subsonic speeds

The OPD_{RMS} for the full turret is mapped out in Figure 4. The top plots demonstrate the mapping in the traditional azimuthal angle and elevation angle coordinate system, while the bottom plots transform the mapping into viewing angle and modified elevation angle space. Figure 5 contains the mapping in just viewing angle space for the hemisphere only turret. For all of the mappings contained in the paper, color features are interpolated between actual data points, given by the grey dots, and as a result, some features in data-sparse areas may be

artifacts of the interpolation. To better understand the way these maps represent the optical performance of the turret and related flow features, Figure 6 splits this data into several bands of the modified elevation angle, β, 30-50 degrees , 50-70 degrees, 70-80 degrees and 80-90 degrees, which are shown in Figures 4 and 5 as green lines.

Analysis will begin with the flat window, located on the left sides of Figures 4 and 5 and in Figure 6. For α < 90°, the aero-optical environment on the full turret is relatively inert, with normalized OPD_{RMS} < 1.5. The aero-optical environment in this range at short timescales is dominated by turbulent structures in the boundary layer over the flat window. For longer timescales, a slow, relative to flow speed timescales, unsteady defocus is present. The necklace vortex and turbulent wake induce changes in the global pressure field that result in local density fluctuation. As the data presented in figures 4 and 5 is short-time averaged to remove defocus due to changing aircraft separation, this unsteady "breathing" in the forward field is also filtered out. As α decreases, OPD_{RMS} also decreases as the turret is looking through a thinner boundary layer closer to the upstream edge of the turret, an effect seen in boundary layer aero-optical studies [9, 10]. The hemisphere-only turret in this regime has a thinner boundary layer compared to the full turret, as shown by reduced OPD_{RMS} values. For 90° < α < 110°, the slope discontinuity of the flat window generates a separation bubble that resides over the flat window. This separation bubble continues to grow as α increases. OPD_{RMS}, however, peaks at a value dependent on β and then decreases. This effect is due to the tip/tilt removal of the wavefronts, and is outlined in more detail in [11]. The β dependence is due to the presence of the necklace vortex near wall of the aircraft influencing the dynamics of the small separation bubble via Biot-Savart induction mechanism. The general behavior of this peak is that it occurs at smaller α as β increases. The same effect is seen in on the hemisphere-only turret, with similar OPD_{RMS} values to the full turret. The dependence of this flow feature solely on the local geometry is the reason for this similarity. However, just as the location of this peak is dependent on β, it also is impacted by turret height for the same reason, and the peak locations vary between the two turret geometries. For α > 110-120°, the flow begins to separate into a fully turbulent wake. The exact separation point is dependent on β, with separation occurring at smaller α for larger β. Comparing the hemisphere-on-cylinder turret to the hemisphere-only turret, separation occurs at approximately the same location, but OPD_{RMS} values in the wake are lower for the hemisphere-only turret. The reduced profile of the turret results in a smaller wake, which reduces OPD_{RMS} values. The exception to this occurs for β > 80°. In this regime, the full turret is looking directly between the two horn vortices of the wake, and OPD_{RMS} is reduced as a result. With the smaller profile turret, the horn vortices are closer to the window, resulting in an increase the OPD_{RMS} compared to the full turret. Similar results along the centerplane were observed in [1].

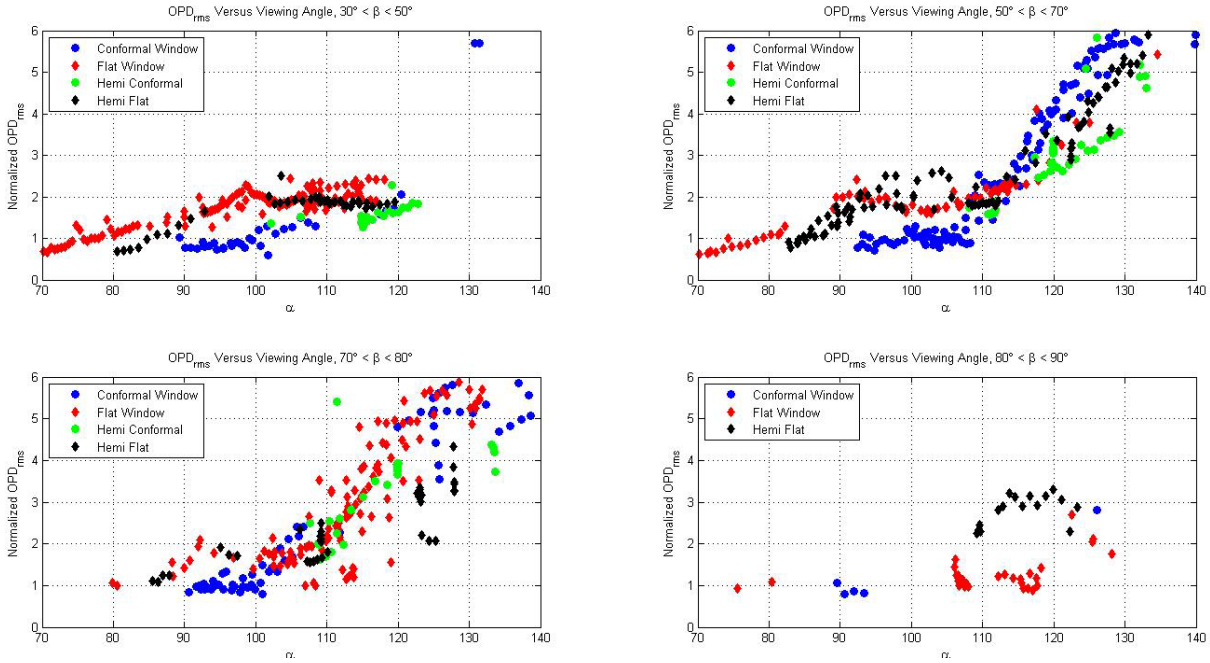

Figure 6. OPD_{RMS} versus viewing angle, broken into bands of modified elevation angle for subsonic flow.

The conformal window exhibits many of the same behaviors as the flat window, with the main difference that the conformal-window does not form the local separation bubble over the aperture. For this analysis, we will

refer to right plots in Figures 4 and 5 and Figure 6. The $\alpha < 110°$ range for the conformal window is mostly dominated by the attached turbulent boundary layer. In this range, OPD_{RMS} values are always lower than for the flat window turret. However, the separation point for the conformal-window turret occurs at a smaller α than for the flat-window turret. To explain this, recall that the separation occurs as adverse pressure gradient forms over the turret. This adverse pressure gradient is a function of the curvature of the turret. The strength of the adverse pressure gradient is related to the slope of the surface of the turret. For a flat window, the slope is constant over the window, and the magnitude of the adverse pressure gradient is constant as well. For the conformal window, the curvature means that even though the slope of the window is the same as the flat window at the center of the aperture, for a given $\alpha > 90°$, the slope becomes larger downstream of the center. The adverse pressure gradient is increasing towards the downstream edge of the window. The overall result of this is that increasing-strength adverse pressure gradient that forms over the conformal window forces separation to occur earlier compared to the flat window. In the separated wake region, OPD_{RMS} values are lower with the hemisphere-only turret due to the smaller wake.

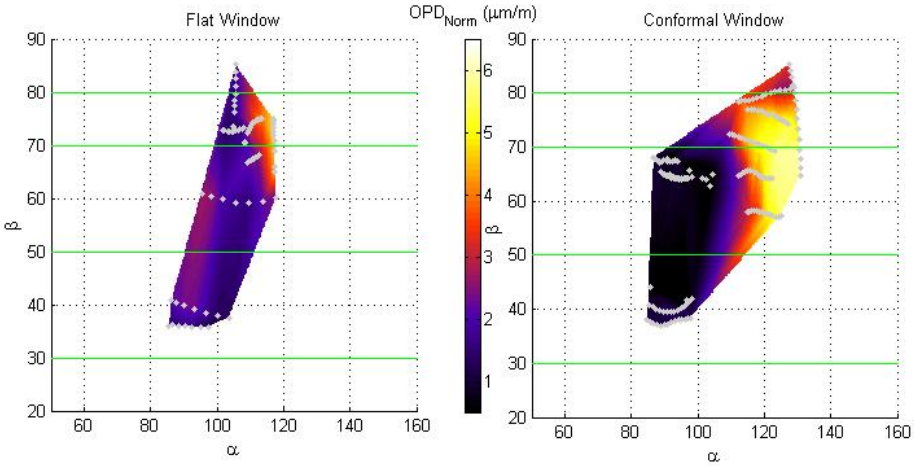

Figure 7. Transonic OPD_{RMS} maps for the hemisphere-on-cylinder turret.

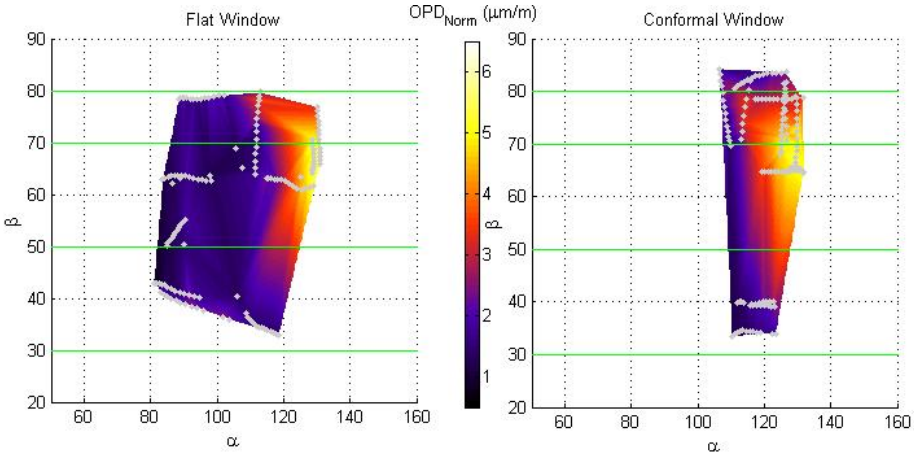

Figure 8. Transonic OPD_{RMS} maps for the hemisphere-only turret.

Transonic speeds

Transonic flow, in regard to optical turret, refers to freestream Mach numbers larger than 0.55, where the flow near the apex of the turret reaches sonic and supersonic speeds [11]. In this regime, a local supersonic region with an ending shock forms on the turret and impact overall optical performance. Figure 7 shows the OPD_{RMS} maps for the transonic regime with a hemisphere-on-cylinder turret. The OPD_{RMS} maps for the hemisphere-only turret are given in Figure 8. As before, the maps of data are broken into same bands of β, as for the subsonic case, to aid in understanding of the different flow features.

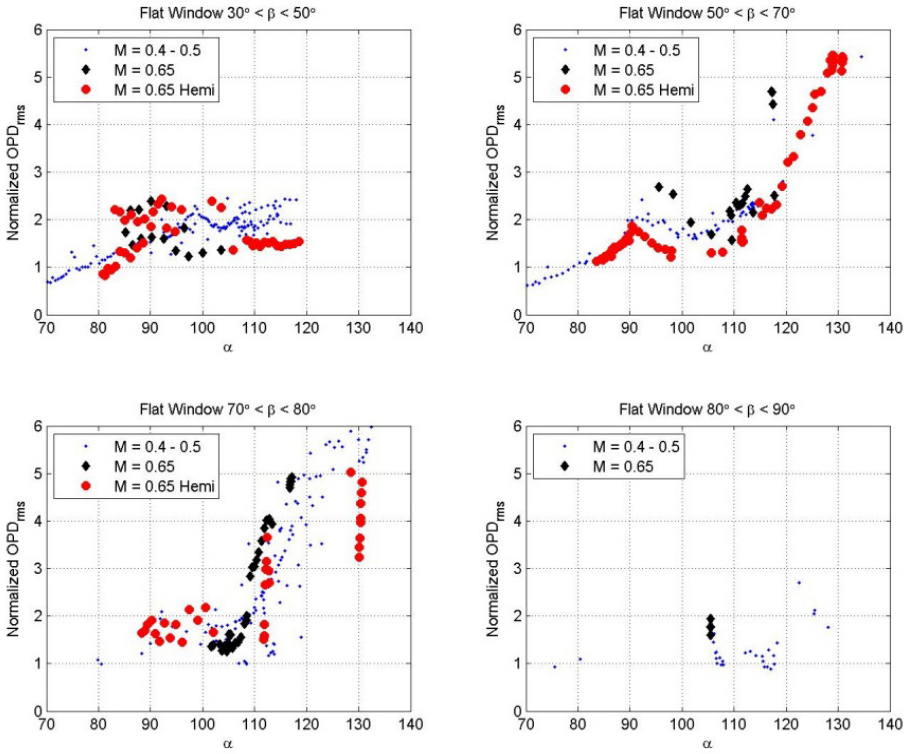

Figure 9. OPD_{RMS} for bands of modified elevation angle at transonic Mach numbers with a flat window.

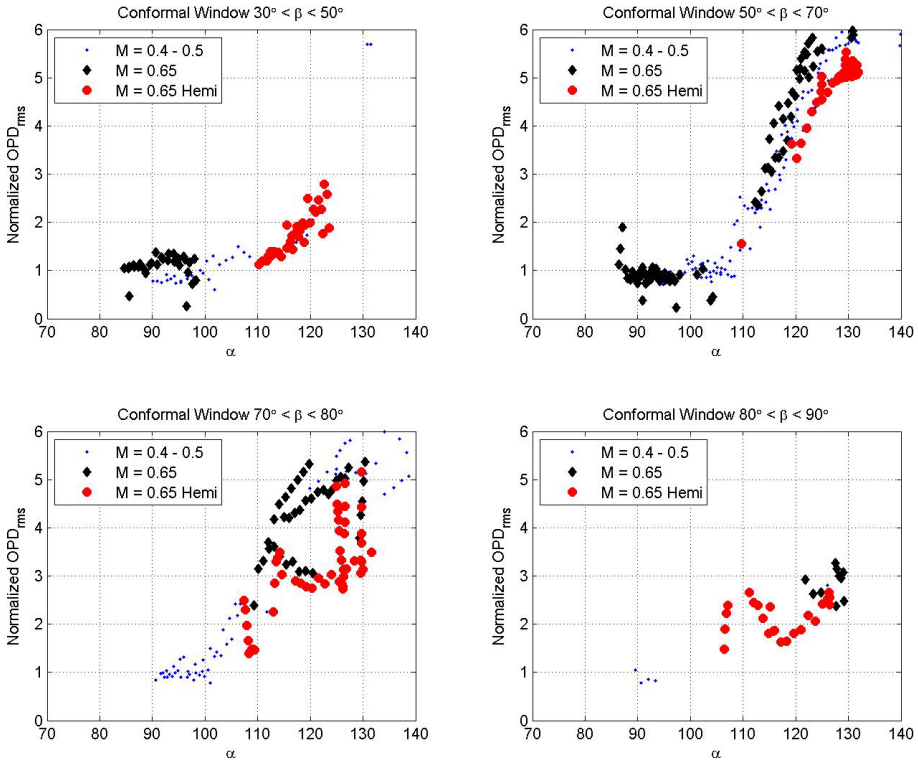

Figure 10. OPD_{RMS} for bands of modified elevation angle at transonic Mach numbers with a conformal window.

Beginning again with the flat window, there are several common features between the transonic and subsonic flow regimes. The flat window transonic data is given in Figures 7 and 8, left and Figure 9. For 85° < α <

110° and β < 50°, there are increases in OPD_{RMS} compared to the subsonic case. These increases are due to a weak shock appearing near the turret apex. This occurs for both the hemisphere-on-cylinder turret and the hemisphere-only turret. The trend of flow separation occurring at smaller α as β increases continues in the transonic regime, as does that of the local maximum in the 90° < α < 110° range due to the separation bubble on the flat window. In the 70° < β < 80° range, separation occurs at smaller viewing angles for the full turret at transonic speeds than subsonic speeds, and OPD_{RMS} values are elevated in the wake, indicating a larger wake at this modified elevation angle.

The conformal turret also shows some similarities to the flat window turret at these angles, see Figure 10. For the full turret, at least, the elevation in OPD_{RMS} in the 85° < α < 100° region is also present with the conformal window. This increase is again due to a weak shock near the turret apex; however, the increase is less pronounced for the conformal window than for the flat window. This indicates an interaction between the flat window and the shock. In the 50° < β < 70° range, the separation point is unchanged, but the OPD_{RMS} values in the wake are elevated slightly for the transonic flow in the full turret case, indicative of a slightly stronger wake. The same trend of lower OPD_{RMS} values for the hemisphere-only turret repeats as well. For β > 80°, the reduced OPD_{RMS} values in the wake region are present. This indicates that the wake is still primarily composed of the two horn vortices in the transonic regime, and in this region the turret is still looking between them.

Shock dynamics at transonic speeds

For the transonic incoming Mach number of 0.65, an intermittent shock was observed over the conformal-window aperture at approximately α = 86°. Figure 11 shows several wavefront snapshots revealing spatio-temporal evolution of this shock; as the density experiences a jump from low values to high values across the shock, the shock is visible as a sharp gradient between the red or high values of wavefront and the blue or low wavefront.

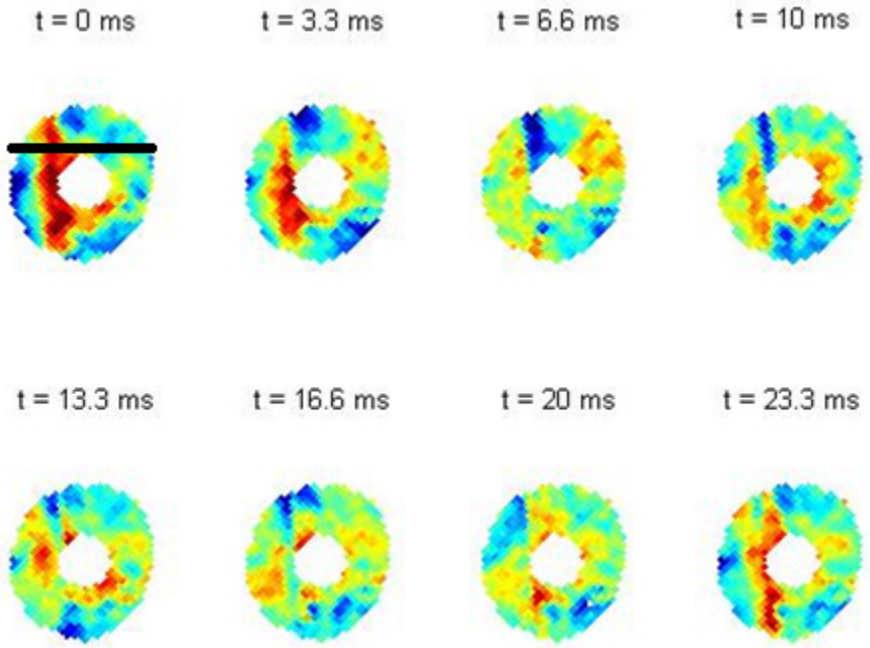

Figure 11. Time evolution of the shock on the aperture. Conformal window turret, M = 0.65, α = 85°, β=40°. The black line, top left, shows the wavefront slice used for analysis.

To better understand the temporal evolution of the shock, temporal evolution of the one-dimensional wavefronts were extracted along the line in the streamwise direction just outside of the obscuration region, as shown schematically in Figure 10, t = 0 ms snapshot. Resulted one-dimensional wavefronts are presented in Figure 12 as a function of the streamwise location, expressed as the viewing angle and time, normalized by the incoming speed and the turret diameter, $T = tU_\infty / D$. Shock-related events can be traced by tear-drop-like blue regions, corresponded to the low-density region just upstream of the shock around the viewing angle of 86 degrees. From Figure 12, intermittent, yet repeatable nature of the shock is evident. By identifying shock occurrences as time instances, where the wavefront locally drops to its lowest value near the viewing angle of 85 degrees, we can compute time intervals between consecutive shock appearances and results are presented in Figure 13 as a histogram. The histogram tail

extends up to ΔT = 5.5. The most probable time interval occurs between shock at approximately ΔT = 2, and the mean time interval is ΔT=2.1. Note that POD-analysis of 2-D wavefront data at transonic speeds [12] revealed that shock-dominant temporal wavefront spectrum has a peak at normalized frequency of $fD/U_\infty = 0.5$, giving the typical (normalized) periodicity of shock events as the inverse of this value, that is $T_{period} = 2$, which is very close to the most probable time interval between shock events.

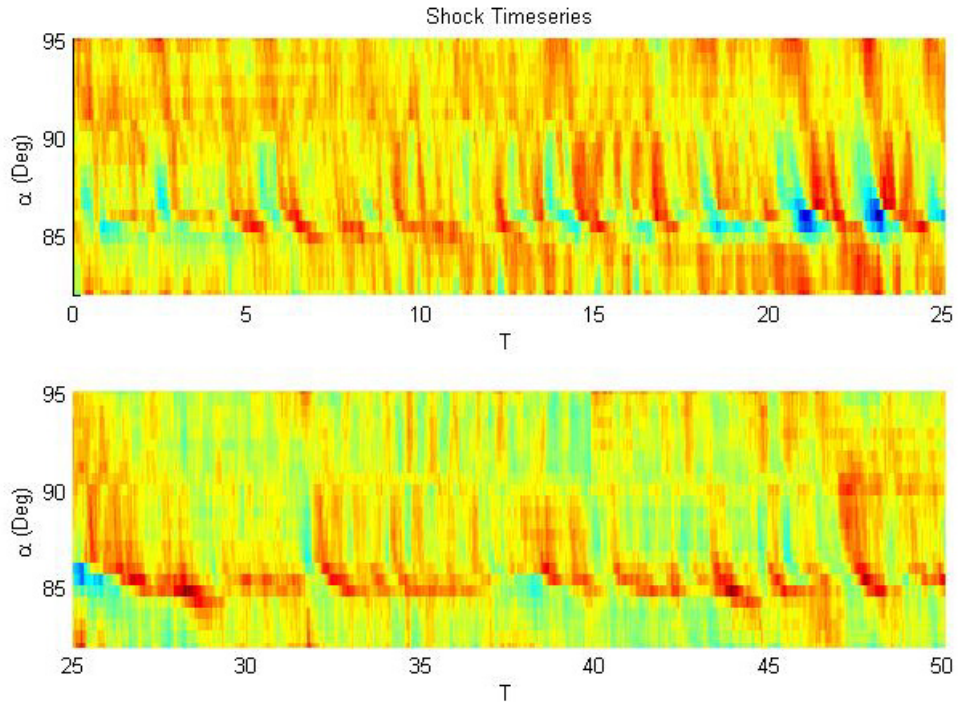

Figure 12. Temporal evolution of 1-dimensonal streamwise wavefronts showing the presence of intermittent shocks on top of the turret.

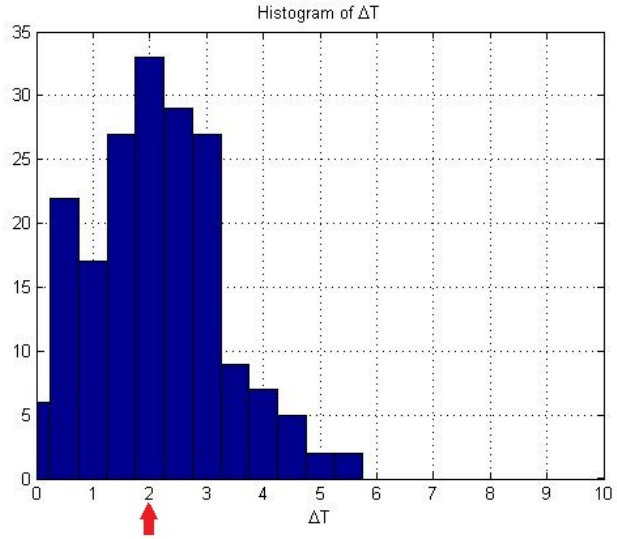

Figure 13. Histogram of the time intervals between consecutive shock events. The most probable event at T = 2 is marked by an arrow.

To better understand the temporal dynamics of the shock-related events, wavefront data were conditionally-averaged in the following way: for each shock-event, identified as above, 1-D wavefronts were extracted between times -1.5T and 1.5T, with T = 0 been at the shock event; wavefronts then were "aligned" such as each shock occurrence corresponds to T = 0 and then wavefronts were ensemble-averaged at every time and the spatial location.

The conditionally-averaged space-time shock-related wavefront is presented in Figure 14. The shock can be seen as a sharp gradient between the blue-region below it and the red-region above it. To better see the shock evolution, several representative times, shown as vertical lines in Figure 14, were selected and corresponding tilt-removed 1-D wavefronts at these times are plotted in Figure 15, left plot. Also, assuming that wavefronts at the very upstream portion of the aperture are not affected by the shock, different tilts were added to each selected wavefront such that wavefronts were forced to be zeros for the first 5 spatial points at the very upstream portion of the aperture; results are re-plotted in Figure 15, right plot. At time T1 = -0.9, the wavefront over the aperture is essentially zero, showing no visible signs of the shock. At time T2 = -0.25, a weak shock appears near α = 86.2 degrees and the wavefront exhibits a linear increase downstream of the shock. The shock is the strongest (by definition of the conditionally-averaged procedure) at T3 = 0, also with the linearly-increasing wavefront downstream of it. Shortly after the shock reaches its maximum strength at T4 = 0.13, the shock starts degreasing in its strength and moving upstream; the wavefront downstream of the shock also grows less, compared to the time instant T3. At the moment T5 = 0.5, the shock moves further upstream with even more decreased intensity; the wavefront essentially stays unchanged downstream of the shock. Finally, at T6 = 0.9, the shock disappears and the wavefront is again almost flat across the aperture.

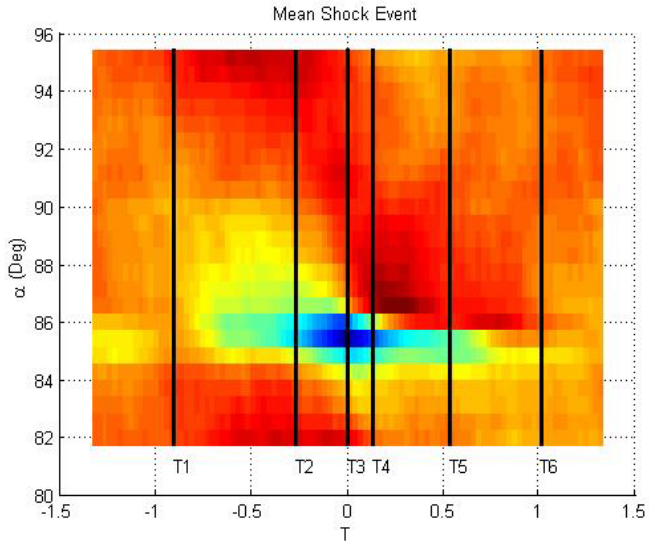

Figure 14. Conditionally-averaged wavefront data to produce an average shock event

Defining the shock strength as OPD jump across it, ΔOPD, the shock strength and its relative position on the turret are plotted in Figure 16, left plot. Before providing a physical explanation of the observed shock behavior, recall that for low subsonic speeds, the pressure is the lowest and therefore the speed is the highest around the viewing angle of 85 degrees [1]. If flow is subsonic everywhere around the turret, the flow speed decreases downstream of 85 degrees. Thus, the subsonic flow is similar to the flow in the convergent-divergent nozzle, where the location of maximum velocity at 85 degrees serves as the throat for the flow on top of the turret. If the incoming speeds is increased until a critical mach number of M = 0.55., the flow near 85 degrees reaches the sonic speed [1]. If the incoming speed is slightly larger than the critical Mach number, which is M = 0.65 for the presented data, the flow is still subsonic upstream of the sonic throat at α = 85 degrees. Remember that the fluidic surface around the turret is not fixed, but experiences temporal-spatial changes due to the evolving boundary layer and the separated region downstream of the turret. Let's say that at the moment T1 the flow reaches the sonic speed at 85 degrees, ,becomes supersonic for a short distance downstream and then, due to the fluidic flow shape, becomes subsonic again, as schematically shown in Figure 16, right. If at some moment T2 the supersonic region increases, it starts forming a small shock near the turret surface some distance downstream of the sonic throat. The velocity before the shock is at a maximum, corresponding to the most negative OPD value; after the shock, density and OPD increase sharply. When at the moment T3 shock gained enough strength, it will cause a premature separation forming immediately downstream of it. The increased separation bubble increases the local fluidic curvature, resulting in reduction of the streamwise velocity and pressure gradient, reduction in the pressure downstream of the shock and forcing the shock to move upstream at the moment T4. When the shock approaches the sonic line at the moment T5, the shock intensity is decreased and the shock eventually disappears at the moment T6, leaving the flow subsonic

everywhere on top of the turret. Then the proposed scenario repeats itself, creating a recurrent pattern of emerging and disappearing shocks. As a final note, the similar shock-evolving mechanism was observed in the shock-induced separation on the wall of a slightly-overexpended supersonic nozzle [13].

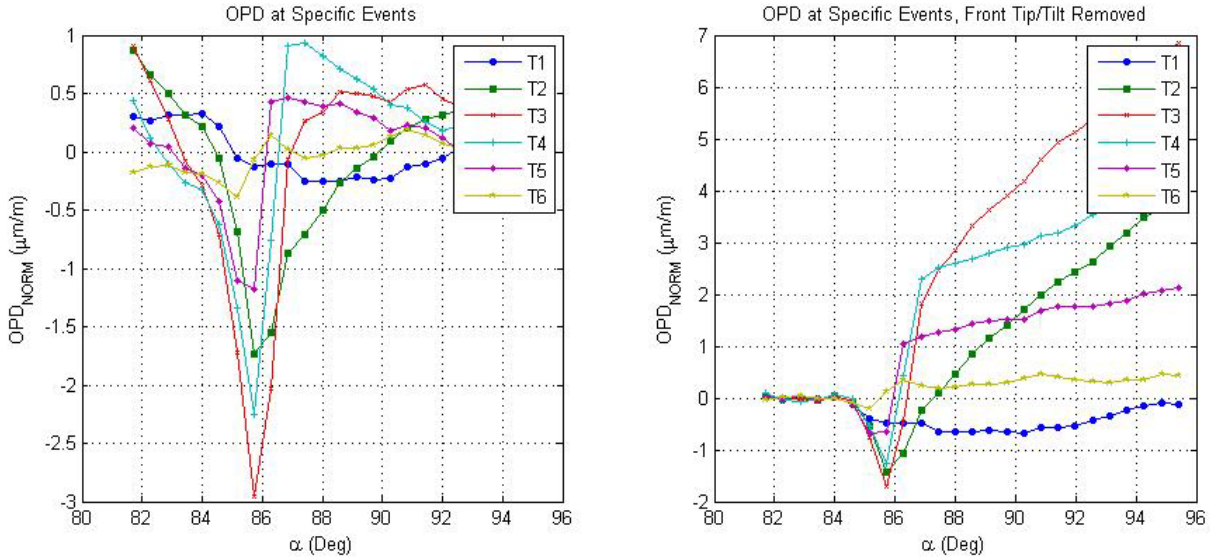

Figure 15. Tilt-removed (left) and tilt-corrected (right) 1-dimensional streamwise wavefronts at selected times, denoted in Figure 14.

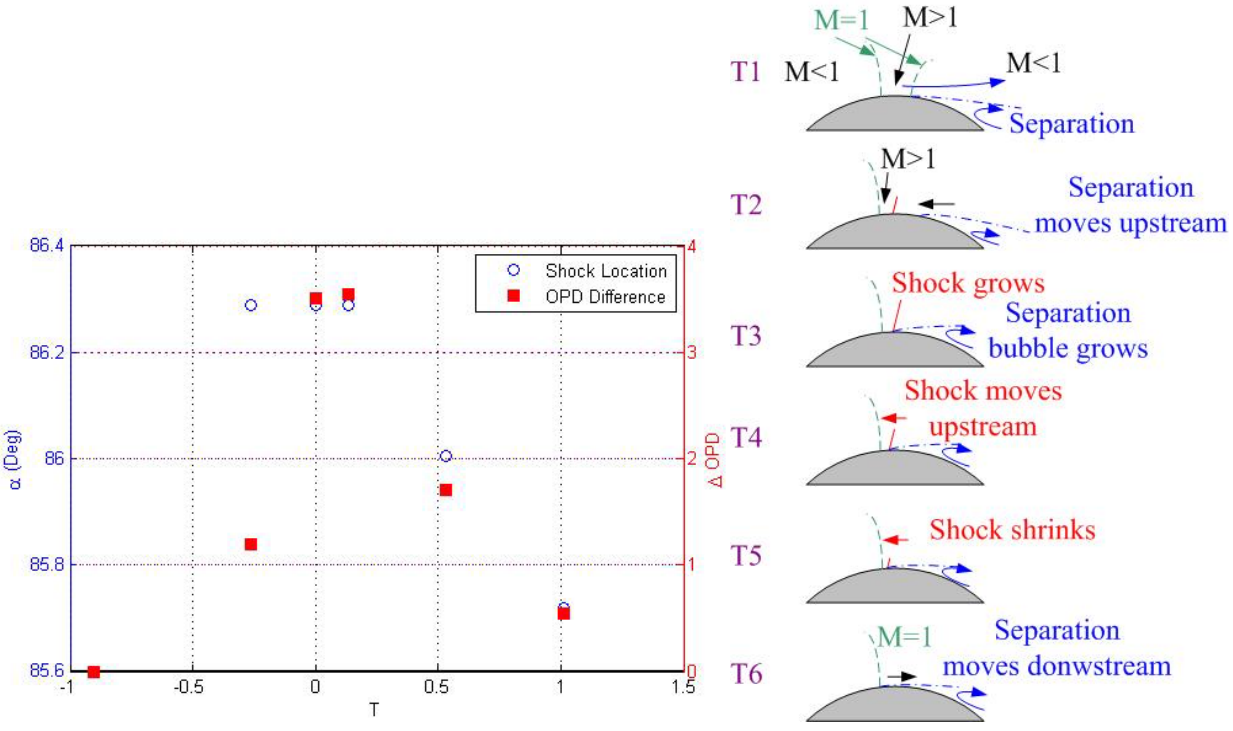

Figure 16. Left: The shock strength, ΔOPD_{NORM}, and the shock location at different times centered around the maximum shock strength. Right: proposed physical mechanism of the shock temporal evolution.

The proposed physical mechanism of the shock dynamics also explains the somewhat surprising relatively-slow shock motion, which is on the order of several characteristic turret times, D/U_∞. As it was shown before, the

shock motion depends on the size and motion of the large separation region downstream of the turret, and it takes several characteristic turret times to change this global flow feature around the turret. Additional cross-correlation measurements between the local shock dynamics and the global separated region will further investigate and improve the proposed mechanism.

V. Conclusions

Using the Airborne Aero-Optics Laboratory, wavefront measurements were performed for both a hemisphere-on-cylinder turret and a hemisphere-only turret. Additionally, both conformal and flat windows were tested, and measurements were obtained at both subsonic and transonic velocities. Through the use of slewing maneuvers, measurements were taken over a large range of viewing angles to allow rapid mapping of the aero-optical performance of the turret in different configurations. The aero-optical environment was characterized through the computation of OPD_{RMS} at each viewing angle. Additionally, shock dynamics were investigated for a weak shock forming upstream of the turret apex in the transonic case.

The hemisphere-only turret mostly exhibits the same general flow features as the hemisphere-only turret. The separation bubble due to the presence of the flat window and the separation point for the wake remain unchanged from the full hemisphere-on-cylinder turret. These effects are dependent only on local geometry changes, and thus are mostly unaffected by the turret height. For $\alpha < 90°$, the hemisphere-only turret exhibits lower OPD_{RMS} values as a result of a smaller boundary layer on the turret. In the separated wake region, $\alpha > 110\text{-}120°$, OPD_{RMS} values are also lower for the hemisphere-only turret as the reduced profile results in a smaller, less turbulent wake. At high elevation angles $\beta > 80°$, both the hemisphere-only turret and the hemisphere-on cylinder turret exhibit reduced OPD_{RMS} values as the aperture looks through the two horn vortices of the wake. However, the hemisphere-only turret has larger OPD_{RMS} in this range as the reduced profile results in the horn vortices being closer to the aperture than with the full turret.

In the transonic regime, the same trends hold: optical performance features due to local geometry remain unchanged while those dependent on global flow features are altered. Both exhibit an increase in OPD_{RMS} for $80° < \alpha < 100°$, due to the presence of the weak shock and for $\alpha > 110°$ due to a shock-related, prematurely-tripped and therefore, larger turbulent wake. For the hemisphere-only turret, OPD_{RMS} values are again smaller in the wake region than for the full turret, as the turret wake is still smaller in this flow regime. Again, for both geometries, separation occurs at a smaller α in the transonic regime.

The dynamics of the weak shock that occurs near the top of the turret in the transonic regime at M=0.65 were investigated. The dynamics of the shock, as well as the extent of its presence on the turret, was found to be non-steady at these speeds. The shock results from the flow becoming locally supersonic shortly downstream of the point of minimum c_p on the turret, at $\alpha = 85°$. As the shock grows in strength, a separation bubble appears downstream of it, with the increased recirculating flow pushing the shock forward towards the sonic line. As the shock reaches the sonic line, it dissipates as the flow is no longer supersonic.

Future work will include the study of flow control devices to improve the aero-optical environment about the hemisphere-on-cylinder turret. Additionally, study of the transonic flow regime will be expanded up to freestream Mach numbers of 0.85. This will allow the study of the evolution of shocks on the turret as a function of Mach number.

References

[1] S. Gordeyev and E. Jumper, “Fluid Dynamics and Aero-Optics of Turrets”, *Progress in Aerospace Sciences*, **46**, (2010), pp. 388-400.

[2] M. Wang, A.Mani and S. Gordeyev, ”Physics and Computation of Aero-Optics”, *Annual Review of Fluid Mechanics*, Vol. **44**, pp. 299-321, 2012.

[3] Gilbert KG, Otten LJ, editors. Aero-optical phenomena, Progress in astronautics and aeronautics series, vol. 80. New York: American Institute of Aeronautics and Astronautics; 1982

[4] C. Porter, S.Gordeyev, M. Zenk and E. Jumper, ”Flight Measurements of Aero-Optical Distortions from a Flat-Windowed Turret on the Airborne Aero-Optics Laboratory (AAOL)”, 42nd AIAA Plasmadynamics and Lasers Conference, 27 - 30 June 2011, Honolulu, Hawaii, AIAA Paper 2011-3280.

[5] N. De Lucca, S. Gordeyev and E. Jumper, “The Airborne Aero-Optics Laboratory, Recent Data”, Acquisition, Tracking, Pointing, and Laser Systems Technologies XXVI, Proceedings of SPIE, Volume 8395, Paper 8395-7, June, 2012.

[6] R. Jelic, S. Sherer and R.Greendyke, ”Simulation of Various Turret Configurations at Subsonic and Transonic Flight Conditions Using OVERFLOW”, AIAA Paper 2012-464, 2012.

[7] J. Tesch, S, Gibson, S. Gordeyev and E. Jumper, "Identification, Prediction and Control of Aero Optical Wavefronts in Laser Beam Propagation", 42nd AIAA Plasmadynamics and Lasers Conference, 27 - 30 June 2011, Honolulu, Hawaii, AIAA Paper 2011-3276.
[8] E Jumper, M Zenk, S Gordeyev, D Cavalieri and M. Whiteley, "The Airborne Aero-Optics Laboratory, AAOL", Acquisition, Tracking, Pointing, and Laser Systems Technologies XXVI, Proceedings of SPIE, Volume 8395, Paper 8395-6, June, 2012.
[9] Cress, J. *Optical aberrations caused by coherent structures in a subsonic, compressible, turbulent boundary layer*, PHD Thesis, University of Notre Dame, (2010)
[10] Smith, AE, Gordeyev, S and Jumper, E, Recent Measurements of Aero-Optical Effects Caused by Subsonic Boundary Layers", Acquisition, Tracking, Pointing, and Laser Systems Technologies XXVI, Proceedings of SPIE, Volume 8395, Paper 8395-11, June, 2012.
[11] S. Gordeyev, J.A. Cress, E. Jumper and A.B. Cain, "Aero-Optical Environment Around a Cylindrical Turret with a Flat Window", *AIAA Journal*, Vol. **49**, No. 2, pp. 308-315, 2011.
[12] D. Goorskey, R. Drye and M. Whiteley," Spatial and Temporal Characterization of AAOL Flight Test Data", Acquisition, Tracking, Pointing, and Laser Systems Technologies XXVI, Proceedings of SPIE, Volume 8395, Paper 8395-8, June, 2012.
[13] B.J. Olson and S.K. Lele,"Large-Eddy Simulation of an over-expanded planar nozzle", AIAA Paper 2011-3908, 2011.